Characterization of land disturbances based on Landsat time series

Shi Qiu*, Zhe Zhu, Xiucheng Yang

Department of Natural Resources and the Environment, University of Connecticut, Storrs, CT 06269, USA.

* Corresponding author: Shi Qiu; E-mail: shi.qiu@uconn.edu

Abstract

We developed a new Object-based Disturbance Agent Classification Approach (ODACA) to characterize land disturbance agents based on Landsat time series. Seven major disturbance agents were characterized, including *harvest, mechanical*, *stress, debris, hydrology*, and *fire*. We first created the land disturbance map by using a modified COntinuous monitoring of Land Disturbance (COLD) algorithm (Zhu et al., 2020), and then established a semi-automated disturbance agent training dataset extraction framework based on existing open-source datasets, with very limited human intervention. The modified COLD algorithm was implemented based on Landsat time series from a single Landsat path to reduce the bidirectional reflectance distribution function effect and issues caused by data density disparity, and the model updating frequency was reduced from every new observation to every three percent of the number of observations used in the previous model updating to improve computational efficiency. Finally, disturbance agents were classified based on ODACA using a Random Forest model with a total of 175 predictor variables that contain rich information in the spectral, temporal, and spatial domains. Accurate land disturbance agent maps were created for five sites in the United States, with an overall accuracy of approximately 99%, and producer's and user's accuracies range from 57 to 100%, depending on specific disturbance agents.

Keywords: Land Disturbance Agent; Characterization; Classification; Change Detection; Time Series Analysis; COLD; ODACA

1. Introduction

Land surface change plays a vital role in global environmental change (Turner II et al., 2007). In the past few decades, the Earth's surface has gone through dramatic changes triggered by various kinds of land disturbances, such as forest harvest, mechanical, debris, hydrology, insect, and fire (Edwards et al., 2014), and the spatial extent and intensity of land disturbances are getting more intensive and extensive (van Mantgem et al., 2009), making detection and characterization of land disturbances of great importance for advancing studies of land surface change and other pressing environmental issues.

Landsat data, with a medium spatial resolution (i.e., 30 m), a high temporal revisit (i.e., 8 days for two satellites), a long history (i.e., 50 years), and the open and free policy (Woodcock et al., 2008; Wulder et al., 2012; Zhu et al., 2019), has become one of the most valuable satellite datasets for monitoring global land surface change (Hansen et al., 2013; Pekel et al., 2016). Based on the Landsat data, many algorithms have been proposed to detect land surface change, such as Disturbance Index (DI) transformation (Healey et al., 2005), Landsat-based detection of Trends in Disturbance and Recovery (LandTrendr) (Kennedy et al., 2010), Vegetation Change Tracker (VCT) (Huang et al., 2010), Composite2Change (C2C) (Hermosilla et al., 2015a), Breaks For Additive Seasonal and Trend (BFAST) Monitor (Verbesselt et al., 2012), Continuous Monitoring of Forest Disturbance (CMFDA) (Zhu et al., 2012), Continuous Change Detection and Classification (CCDC) (Zhu and Woodcock, 2014), Continuous monitoring of Land

Disturbance (COLD) (Zhu et al., 2020), supervise-classification-based approach (Hansen et al., 2014), and multiple change detection ensemble method (Bullock et al., 2019; Healey et al., 2018). Some of them have been successfully implemented to generate national or global change products (Brown et al., 2020; Hansen et al., 2013). However, most of them were designed for detecting land cover and land use change, and only very few algorithms were proposed to detect land disturbance. Moreover, most of the disturbance detection algorithms were only focused on disturbance within a single cover type, such as forest disturbance (Healey et al., 2018, 2005; Huang et al., 2010; Kennedy et al., 2007; Zhu et al., 2012). Meanwhile, the COLD algorithm, built upon the success of the CCDC algorithm, can continuously detect land disturbance occurring on all kinds of land surfaces based on dense Landsat time series (Zhu et al., 2020).

It is useful to know where and when land disturbance happened, but it is also beneficial to know why they occurred, or the identification of the disturbance agent. For a long time, change agent mapping has been focused on single a single agent, such as fire (Roy et al., 2019), water dynamics (Pekel et al., 2016), and insect infestation (Ye et al., 2021). Recently, built on the well-development of time series based change detection algorithms, the combined use of change magnitude, spectral information in pre- and post-change, topography, patch metrics (e.g., size and shape), and landscape context information has made identification of multiple forest disturbance agents possible (e.g., harvest, fire, insect, and wind) (Coops et al., 2020; Hermosilla et al., 2015b; Schroeder et al., 2017; Sebald et al., 2021; Zhang et al., 2022). Those studies usually need a huge amount of labor work to interpret training data based on high-resolution images and are not able to extend to non-forested lands.

Table 1

Definition of the classification system of land disturbance agents.

Categories	Definitions
Harvest	Forested land, where trees are harvested by human activities, such as clear cut, selective logging, salvage logging, etc.
Mechanical	Non-forested land, where human activities are the major cause of the disturbance, such as agriculture practice, urban expansion, modification, and intensification.
Stress	Vegetated land, where the condition of trees or other woody vegetation is changed to a less favorable status by natural factors, such as insect infestation, disease, and drought.
Debris	Land scattered with debris of natural or artificial materials that caused by hurricanes, tornados, landslides, volcanoes, etc. Note that the movement of materials in riverine systems is labeled as hydrology.
Hydrology	Long-term or short-term transitions from land to water or from water to land caused by flooding, sea-level rising, damming, etc.
Fire	Fire burnt areas on all land surfaces, such as forests, shrublands, or grasslands.
Other	Land altered due to other causes, mostly due to vegetation regrowth and year-to-year climate variability.

There are various kinds of the definition of land disturbance agents, and in this study, we used a more general definition of land disturbance, including *harvest*, *mechanical*, *stress*, *debris*, *hydrology*, *fire*, and *other*. Table 1 describes the definition of each of them, which mainly follows the USGS Land Change Monitoring, Assessment, and Projection (LCMAP) program (Brown et al., 2020; Pengra et al., 2020; Xian et al., 2022).

Therefore, the main purpose of this study is to design automated algorithms to characterize land disturbance agents based on Landsat time series across the conterminous United States (CONUS), such as *harvest*, *mechanical*, *stress*, *debris*, *hydrology*, and *fire* (Table 1).

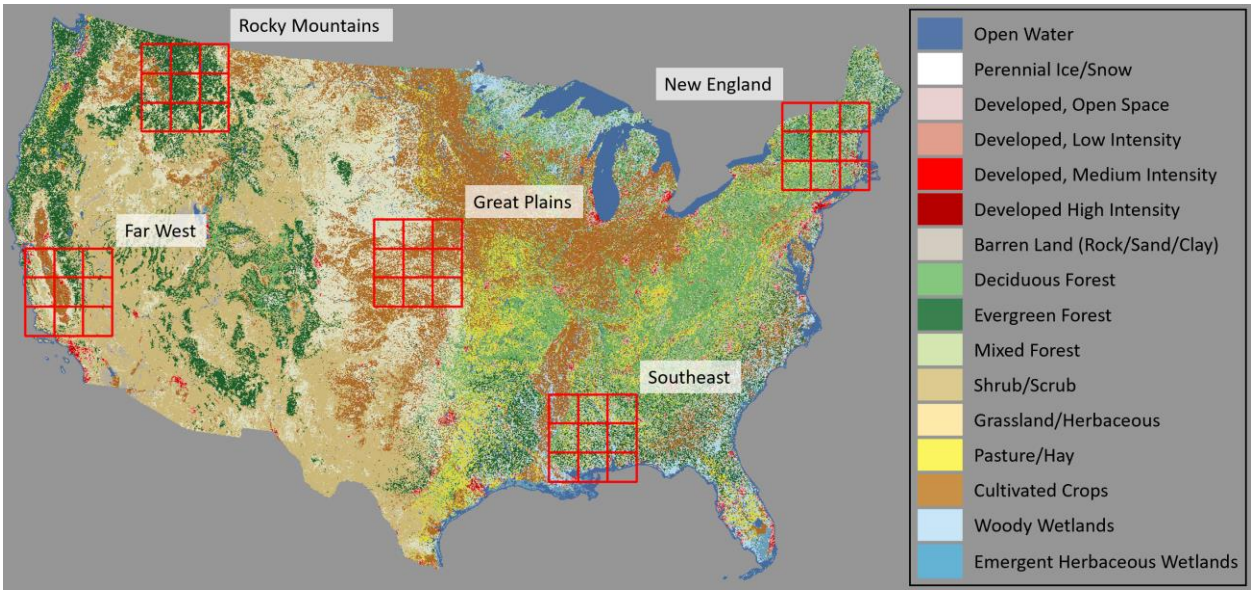

Figure 1. Distribution of five study sites in the United States. Each site is covered by 3-by-3 Landsat Analysis Ready Data tiles (red squares). The background is the 2016 National Land Cover Dataset (Jin et al., 2019).

2. Study area and data

2.1. Study area

We selected five study sites to test our algorithms, in which each site contains 3-by-3 Landsat Analysis Ready Data (ARD) tiles (Dwyer et al., 2018) (Figure 1). The study sites are in different parts of the CONUS (New England, Southeast, Great Plains, Rocky Mountains, and Far West sites), with diverse topography and environmental conditions. The major land disturbances in the New England site include forest harvest in the north, mechanical activities in urban areas (e.g., Metro Boston), insect outbreaks (e.g., gypsy moth), hydrology, and debris caused by tornado. The Southeast site was selected due to frequent hurricanes that caused debris, as well as the intense forest harvest activities. In the Great Plains area, agricultural activities are the dominant disturbance type, and large areas of grasslands and wetlands are frequently disturbed by year-to-year climate variability (Zhou et al., 2019). The Rocky Mountains site is characterized by high mountains, where the major land cover is forest, but often affected by insects (e.g., bark beetle) and fire events. The land disturbance in the Far West site mainly involves mechanical activities

in urban and agricultural areas, large fires in mountains, large areas of grasslands/shrublands frequently disturbed by climate variability, and debris caused by several major earthquakes.

2.2. Landsat Data

USGS Landsat Collection 1 Analysis Ready Data (ARD) were used as the major input datasets. The Landsat ARD analyzed here include Landsats 4–5 Thematic Mapper, Landsat 7 Enhanced Thematic Mapper Plus, and Landsat 8 Operational Land Imager /Thermal Infrared Sensor data. They were provided with tiles of 5000 × 5000 30-m pixels under the Albers Equal Area Conic projection. For each ARD tile, surface reflectance of blue, green, red, NIR, and two SWIR bands, Brightness Temperature (BT) of Thermal Infrared (TIR) band, and Quality Assessment (QA) band were used in the analysis, in which the surface reflectance data were produced using the Landsat Ecosystem Disturbance Adaptive Processing System (LEDAPS) Algorithm (Masek et al., 2006) and the Landsat Surface Reflectance Code (LaSRC) (Vermote et al., 2016), and the QA band that provides the per-pixel information on cloud, cloud shadow, and snow/ice was based on the Function of mask (Fmask) algorithm (Zhu et al., 2012; Zhu et al., 2015a). All Landsat images with cloud and shadow cover less than 100% between 1982 and June 2020 were downloaded based on the machine-to-machine Application Programming Interface (API) of USGS Earth Explorer.

2.3. Auxiliary data

The auxiliary data for disturbance agent classification consisted of Digital Elevation Model (DEM), slope, and aspect. The global 30-m DEM data were derived from Shuttle Radar

Topography Mission (SRTM), due to their relatively high accuracy (Rodriguez et al., 2006). The slope and aspect were derived from the DEM data.

2.4. Land disturbance agent related open-source datasets

We collected the disturbance agent training data based on multiple existing open-source datasets related to land disturbance, which include USGS LANDFIRE public events geodatabase (Rollins, 2009), Monitoring Trends in Burn Severity (MTBS) (Eidenshink et al., 2007), USGS Land Cover Trends (LCT) (Loveland et al., 2002), National Land Cover Database (NLCD) Science Research Products with information on Forest Transition Classes (FTC) (Jin et al., 2019), European Joint Research Centre's Global Surface Water (JRC GSW) (Pekel et al., 2016), survey data such as Insect and Disease Survey (IDS) (Johnson and Wittwer, 2008), and disaster event reports such as NOAA Severe Weather Database (SWD) and NASA Global Landslide Catalog (GLC) (Kirschbaum et al., 2010). Each of them was used as a base layer to help with automated generating training data of land disturbance agents.

2.5. Calibration and validation samples

We generated two sets of reference samples to calibrate the agent classification algorithm (e.g., selecting classification strategy and optimal thresholds) and to conduct accuracy assessments for the land disturbance agent maps, respectively. The two reference sample sets were collected independent of each other, but based on the same response design to interpret the land disturbance agent. In particular, the disturbance agent for each sample was determined by using the Area Estimation & Accuracy Assessment (AREA2) tool at Google Earth Engine, which can display the time series of Landsat images (Arévalo et al., 2020; Bullock et al., 2020, 2019).

Available historic high-resolution images from Google Earth and previously mentioned open-source datasets (e.g., MTBS and IDS) (Section 2.4) were also used to help the human interpretation.

The calibration samples included a total of 450 pixels, that were randomly selected within the COLD disturbance locations over the 45 Landsat ARD tiles (10 samples for each tile). Since the classification algorithm does not be focused on disturbance detection, we excluded commission errors of disturbance detection caused by the COLD algorithm in calibrating the ODACA algorithm.

On the other hand, the validation samples were created by following the "good practice" recommendations described by Olofsson et al., (2014). In this study, we randomly selected a total of 1,525 samples based on the stratified random sampling constructed from the annual land disturbance agent maps between 1985 and 2020. In this stratification, the individual reference sample represents not only a location on the ground but also a place in time. Considering that agent strata were rare classes compared to the non-disturbance areas, a minimum of 100 reference samples were allocated into these seven rare disturbance agents. The remaining 525 reference samples were allocated to *no disturbance* stratum. The samples with low interpretation confidence were excluded (see Table 4 for the statistic of validation samples).

3. Methods

Figure 2 shows the flowchart of algorithms for characterizing land disturbance. We first implemented the modified COLD algorithm to detect any kinds of land disturbances at pixel

level based on Landsat time series extracted from single Landsat path, and then created disturbance objects for each calendar year (Section 3.1). Next, the Object-based Disturbance Agent Classification Approach (ODACA) was used to attribute the land disturbance agent, in which the disturbance agent training data were generated from existing open-sources datasets (Section 3.2) and used to train the iterative random forest classifiers with 175 predictor variables (Section 3.3). The output results consist of annual disturbance agent maps with location, time, and agent, and accuracy assessment following the good practices (Olofsson et al., 2016) (Section 3.4).

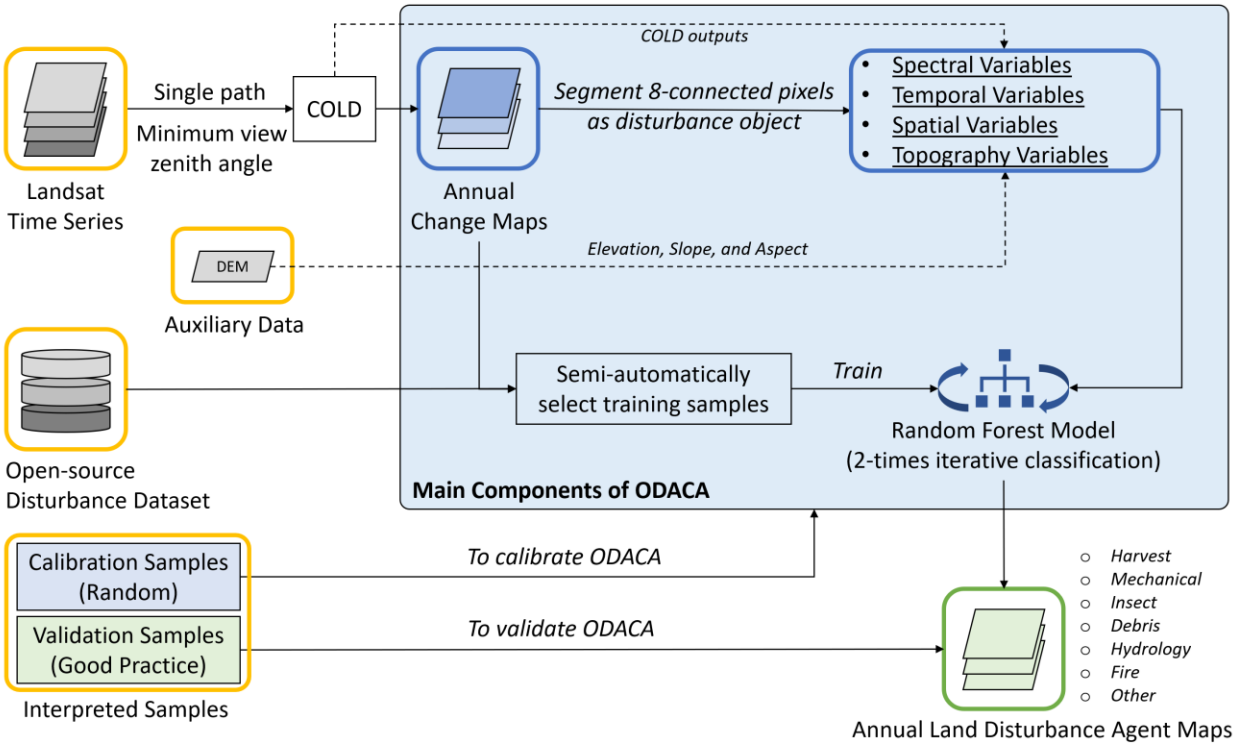

Figure 2. Flowchart of detecting and characterizing land disturbance in this study. The main components of ODACA are described in the large blue rectangle. COLD: COntinuous monitoring of Land Disturbance. ODACA: Object-based Disturbance Agent Classification Approach.

3.1. Detection of land disturbance

The COLD algorithm is able to provide accurate per-pixel land disturbance information based on dense Landsat time series. For each pixel, the inputs are consisted of the times series of seven spectral bands, such as surface reflectance of blue, green, red, NIR, SWIR1 and SWIR2 bands, as well as BT of TIR band.

$$\hat{\rho}_{i,x} = a_{0,i} + \sum_{k=1}^{3}\{a_{k,i}\, cos(\frac{2\pi k}{T} t) + b_{k,i}\, sin(\frac{2\pi k}{T} t)\} + c_{1,i} \quad (1)$$

Where,

t: Julian date

i: The *i*th Landsat spectral band

k: Temporal frequency of different harmonic component (*k* = 1, 2, and 3).

T: The average number of days per year (*T* = 365.25)

$a_{0,i}$: Coefficient for capturing the overall value for the *i*th Landsat spectral band

$a_{k,i}$, $b_{k,i}$: Coefficients for capturing the intra-annual change for the *i*th Landsat spectral band

$c_{1,i}$: Coefficient for capturing the inter-annual change for the *i*th Landsat spectral band

$\hat{\rho}_{i,x}$: Surface reflectance for the *i*th Landsat spectral band at *x* Julian date based on model prediction.

The core of the COLD algorithm is to predict the surface reflectance of each spectral band ($\hat{\rho}$) based on a Harmonic time series model (Eq. 1), using the Least Absolute Shrinkage and Selection Operator (LASSO) with a lambda of 20 (Tibshirani, 2011). A change is identified when consecutive six reflectance differences ($\Delta\rho$), between actual observations (ρ) and model predictions ($\hat{\rho}$), are larger than a threshold of change probability of 0.99 (Zhu et al., 2020). Once

a change is identified, a new Harmonic model will be estimated. If no change is confirmed, new Landsat observations will be appended to update the model. In the COLD algorithm, only five Landsat spectral bands, such as the green, red, NIR, SWIR1, and SWIR2 bands, are used to detect change, but all spectral bands will be used for estimating their specific time series models.

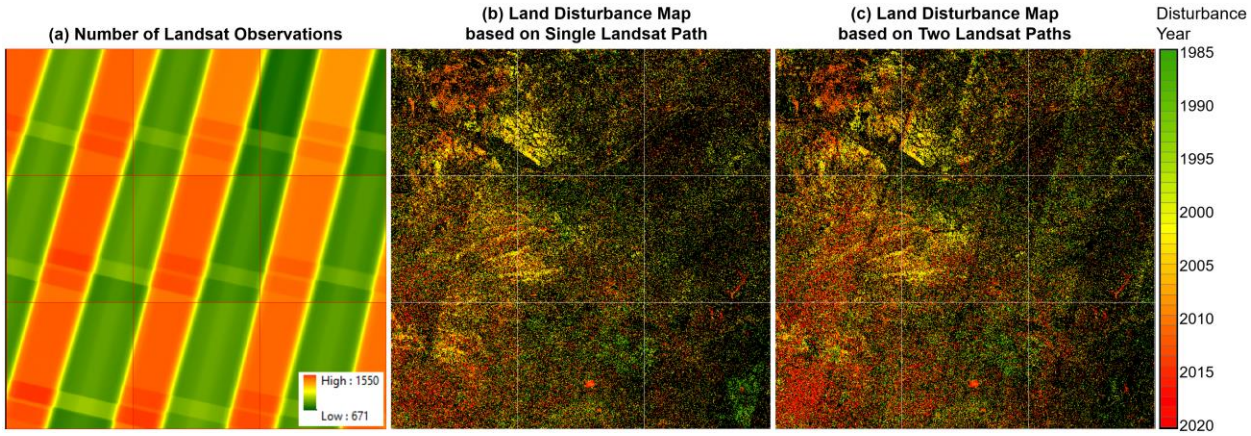

Figure 3. Land disturbance maps based on Landsat observations from a single path (Figure 3b) versus they are based on all Landsat ARD (Figure 3c) for Great Plains in 3-by-3 Landsat ARD tiles. This area includes large areas of land disturbance caused by agriculture practices and climate variability, which are particularly sensitive to the difference of data density of Landsat time series (Figure 3a).

One of the issues with the original COLD algorithm is the large inconsistency of disturbance maps between the adjacent Landsat path overlap and non-overlap regions (Figure 3c), due to large differences in temporal density (Figure 3a) and the Bidirectional Reflectance Distribution Function (BRDF) effects (mostly caused by different view zenith angles) (Zhu and Qiu, 2022, preprint paper). We modified the COLD algorithm from using all Landsat ARD (including overlap regions) to only using Landsat observation from a single path, in which Landsat ARD with the smallest view zenith angles will be selected as the inputs for COLD. This will ensure a homogeneous change map at a large-scale (Figure 3b). Note the density adjustment approach (Zhu et al., 2020) is not needed anymore when using Landsat time series from a single path. Another modification of the COLD algorithm is to reduce the model updating frequency from every new observation to every 3% of the number of observations used in previous model

updating. This modification can greatly (>60%) reduce the computation time and almost achieve the same accuracy as the original COLD algorithm based on the same reference sample provided in Zhu et al., (2020).

3.2. Characterization of land disturbance agent

An Object-based Disturbance Agent Classification Approach (ODACA) was developed to attribute land disturbance agents detected by the modified COLD algorithm. The annual per-pixel land disturbance maps derived from the modified COLD algorithm were first aggregated into separate disturbance objects based on 8-connected directions under the assumption that land disturbance events are spatially connected within a relatively short time (e.g., one year). We removed disturbance objects that are less than four Landsat pixels (~0.4 ha), as this is usually the smallest unit that can be reliably mapped by Landsat data (Dobson, 1995).

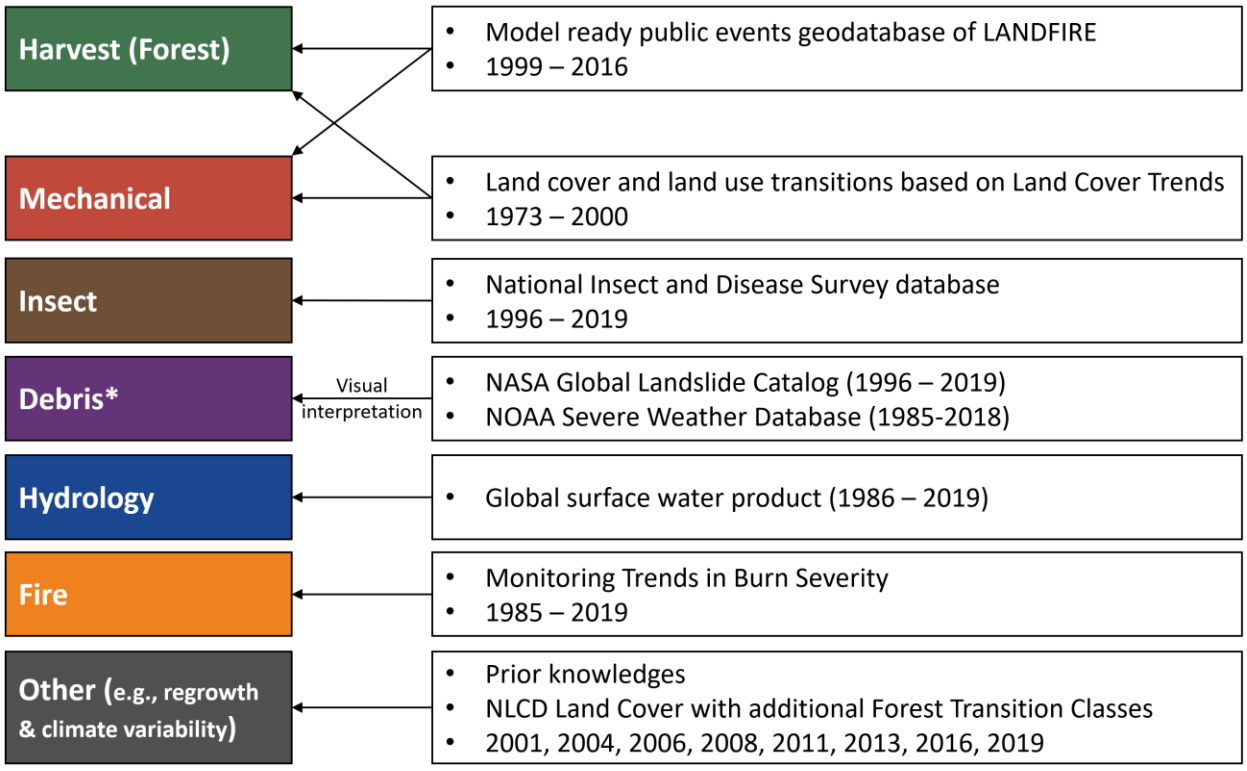

Figure 4. Illustration of disturbance sample generation from the existing open-source dataset. *Debris* samples are relatively few and were carefully interpreted based on NASA Global Landslide Catalog and NOAA Severe Weather Database.

3.2.1. Extracting disturbance agent training data based on open-source datasets

We assembled existing open-source datasets to build a comprehensive training dataset with multiple disturbance agents (Figure 4). Based on existing disturbance reference datasets (i.e., LANDFIRE and MTBS), survey data (i.e., IDS), and LCLU maps (i.e., LCT, NLCD, and GSW), as well as with prior knowledge (e.g., small change magnitude for *stress* and greener direction in *other* like vegetation regrowth), we can produce a record of potential disturbance agent locations (hereafter referred to "potential agent map") for each agent type for each year. Later, the agent of each disturbance object was determined based on the overlap between the disturbance object identified by the modified COLD algorithm and the potential agent maps derived from the open-source dataset, and only when more than half of the pixels within each disturbance object were filled by the potential agent maps, the agent can be assigned successfully. When multiple agents were in the same object, a majority rule was applied. This approach was used to generate the training samples for most of the land disturbance agents, but we carefully interpreted the *debris* samples based on disaster event reports (e.g., hurricane, tornado, and landslide) from NOAA SWD and NASA GLC (Kirschbaum et al., 2010) to guarantee the training data quality, as not all area will show up as *debris* within the trajectory of hurricane, tornado, and landslide. Table 2 shows the disturbance agent training data for each study site, which were used to train the classification model.

Table 2. Statistics of disturbance agent training data (# of pixels) for each study site.

Site	Harvest	Mechanical	Stress	Debris	Hydrology	Fire	Other
New England	46,556	42,050	14,424	16,148	21,044	0	19,216
Southeast	183,815	113,418	107	477,959	333,021	0	1,611,880
Great Plains	166	366,273	0	0	169,014	196,202	5,974,637
Rocky Mountains	468,218	151,045	3,405	67	59,799	10,221,023	587,655
Far West	45,181	4,424,306	14,497	929	502,381	12,283,243	72,129,026
Total	743,936	5,097,092	32,433	495,103	1,085,259	22,700,468	80,322,414

3.3.2. Predictor variables

A total of 175 predictor variables for agent classification were calculated based on the outputs of the modified COLD algorithm, topographic data, and object-based metrics of disturbance objects (Table 3).

Table 3
Predictor variables for classifying land disturbance agents. There is a total of 175 variables.

Class	Input Variables	Number
During-change	Change time	1
	Change magnitude (7 bands)	7 (1 variable * 7 bands)
	Change magnitude trend and variation (Slope, RMSE)	14 (2 variables * 7 bands)
	Change interval	1
	Change frequency (times per year)	1
Pre-change	Time series models of pre-change (i.e., a_0, a_1, b_1, a_2, b_2, a_3, b_3, and RMSE)	49 (7 variables * 7 bands)
Post-change	Time series model of post-change (i.e., a_0, a_1, b_1, a_2, b_2, a_3, b_3, and RMSE)	49 (7 variables * 7 bands)
Topographic	Elevation	1
	Aspect	1
	Slope	1
Patch	Standard deviation of change time	1
	Standard deviation of change magnitude	7 (1 variable * 7 bands)
	Standard deviation of change interval	1
	Area	1
	Core area index	1
	Related circumscribing circle	1
	Contiguity index	1
	Core area	1
	Euclidean nearest-neighbor distance	1
	Fractal dimension index	1
	Radius of gyratio	1
	Number of core areas	1
	Perimeter-area ratio	1
	Perimeter	1
	Shape index	1
	Elevation range	1

There were 122 predictor variables directly calculated from the modified COLD algorithm, which include information extracted during-change, pre-change, and after-change for every change event at the pixel level. Figure 5 illustrates the modified COLD results for a pixel in New

England Area that has undergone a change in 2016 caused by *stress* (gypsy moth). For a change event, the modified COLD algorithm created a time series model before change (pre-change model), a time series model after change (post-change model), and during-change information for each spectral band. The pre-change and post-change models indicate the land surface before and after a disturbance has happened, respectively. The during-change information includes change magnitude, as well as change magnitude trend and variation. Most of the COLD output variables have been already well-documented in Zhu et al. (2020), except for change magnitude trend and variation. The change magnitude trend represents trend of the reflectance differences ($\Delta\rho$) between the model predictions and the actual observations for the six consecutive observations during the change process. A linear model based on ordinary least square regression is used to estimate the trend, and the change magnitude variation is calculated based on the corresponding Root Mean Square Error (RMSE), which is to measure the regression uncertainty. Based on the same pixel as shown in Figure 5, Figure 6 illustrates how the change magnitude trend and variation is determined based on the reflectance difference (between model prediction and observation) of six consecutive Landsat observations. In this specific case, the trend and variation values can provide rich information on the immediate change procedure of the natural vegetation restoration after an insect attack, which could be valuable inputs for disturbance agent attribution. At the same time, we also used change time to indicate when (day of year) a disturbance happened, change interval to describe how long the disturbance lasted, and change frequency to measure how often the disturbance occurred, as we think all these change information could be extremely helpful for disturbance agent attribution. Moreover, we also included three topographic predictor variables, including elevation, slope, and aspect, all of

which have already shown promise in classifying disturbance agents (Kennedy et al., 2015; Oeser et al., 2017).

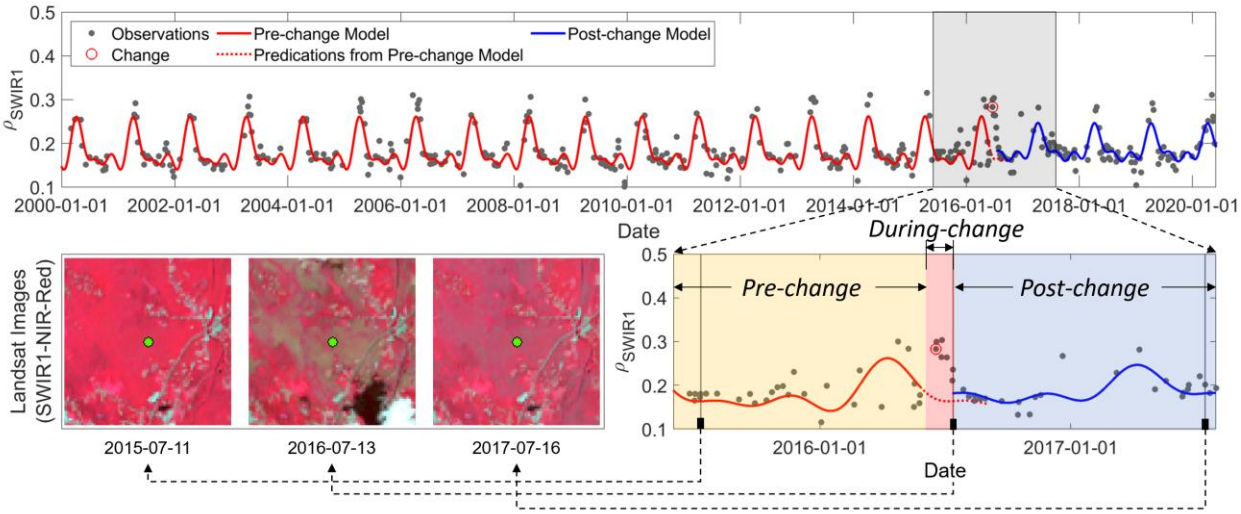

Figure 5. An illustration of the modified COLD algorithm for a forest pixel (Long: -71.6430, Lat: 41.9749). Upper panel shows the Landsat time series from 2000 to 2020, and a change caused by the gypsy moth is identified in 2016 by the COLD algorithm. Lower-right panel enlarges the during-change process and shows the corresponding Landsat time series. Lower-left panel shows three summer Landsat images collected pre-change in 2015, during-change in 2016, and post-change in 2017, respectively. Note the Landsat images in the lower-left panel can be compared directly since they are displayed using a same stretch, and the area affected by the gypsy moth is most noticeable in the 2016 image.

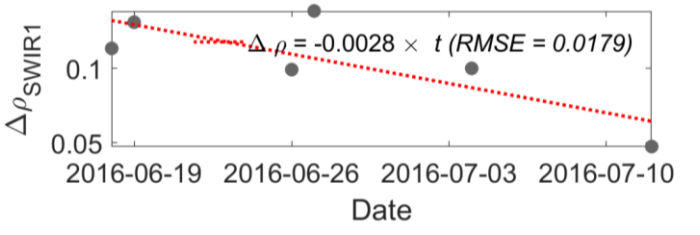

Figure 6. The slope and RMSE of change magnitude of six consecutive observations during change for the same pixel shown in Figure 5. The insect (gypsy moth) infestation initially resulted in a spectral difference, but after this event the differences began decrease continuously due to vegetation recovery.

Based on the assumptions that different disturbance agents have different spatial patterns, we also computed the spatial patch metrics for each disturbance object. For instance, according to change time, change magnitude, and change interval of each pixel in the same disturbance

object, we computed their standard deviation values to describe their texture for each disturbance object. On the other hand, we calculated twelve spatial predictor variables to describe the spatial pattern of disturbance object, such as size, form, and shape, using FRAGSTATS -- a spatial pattern analysis program for quantifying landscape structure (Hesselbarth et al., 2019; States, 1995), which has been widely used to map land cover land use (Fan and Myint, 2014) as well as forest disturbance agent attribution (Sebald et al., 2021). In addition, since the range of elevation could also influence the type of disturbance agent, for example, debris caused by landslide would be more likely to occur in regions with large elevation difference, and therefore, we computed the elevation range for each disturbance object.

3.3.3. Classification strategy

In ODACA, a supervised Random Forest Classifier (RFC) (Breiman, 2001) is applied for attributing disturbance agents, and a total of 100 decision trees were used for balancing computation efficiency and classification accuracy (Rodriguez-Galiano et al., 2012). The training data are pixel-based (Table 2), instead of at the object-level, since the former can provide many more training samples with large variations of spectral information. For training pixels within the same object, they will share the same values in the patch-based variables.

Optimized local and global training data selection. In each study site (3-by-3 Landsat ARD tile, we trained the RFC based on a hybrid training data selection strategy, in which 60% of them were locally selected from the nine ARD tiles in this same study site (hereafter referred to as "local sample"), and the remaining 40% of them were extracted from the tiles in other four sites (hereafter referred to as "global sample"). The combined use of the local and the global training

samples can avoid the issue of lacking enough training data for rare disturbance agents in certain places and at the same time maintain enough "localness" in the selected training data. The two proportions were determined based on the algorithm performances against the calibration samples, in which 40% from "global" and 60% from "local" achieved the highest overall accuracy (Figure 7). In addition, as our target was to determine the agent of each disturbance object, we used the well-trained RFC to classify all pixels within each disturbance object and applied a majority vote to determine the final agent for the disturbance object.

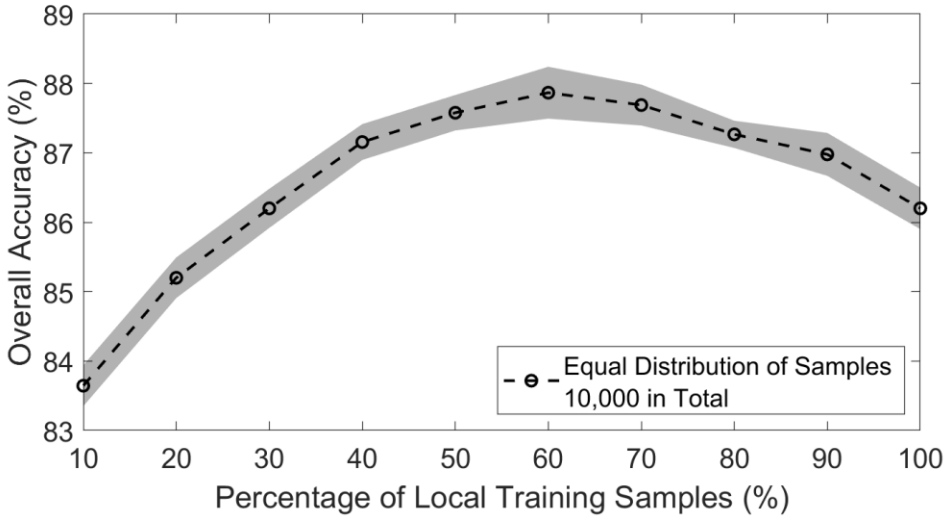

Figure 7. Analyses of the impacts of percent of local training data (x-axis) and global training data (100 – x-axis) used in disturbance agent classification.

Optimized class proportion training data selection. Usually, the number of training data selected for each class should be based on the corresponding class area proportion with some limits on some dominant classes (e.g., class proportion > 40%) and some benefits for some rare classes (e.g., class proportion < 3%) (Zhu et al., 2016). However, there is no way to know the class proportion before we have a map of it. To solve this chicken-and-egg dilemma, we created a novel iterative RFC procedure, in which we first used the equal distributional training data (all classes have the same number of training data) to create the first preliminary disturbance agent

classification map, and then, we will use the proportion information from this preliminary map (with a minimum proportion of 3% and a maximum proportion of 40%) to extract training data based on mapped class proportion to train a new RFC to classify the final land disturbance agent map.

Optimized total number of training data. We also tested the impact of the total number of training data on land disturbance agent classification based on the above two optimized strategies, and we found that the classification overall accuracy continues to increase when the number of training samples increases, and plateaus between 5,000 and 10,000 pixels. Therefore, a total of 10,000 training samples were selected in ODACA.

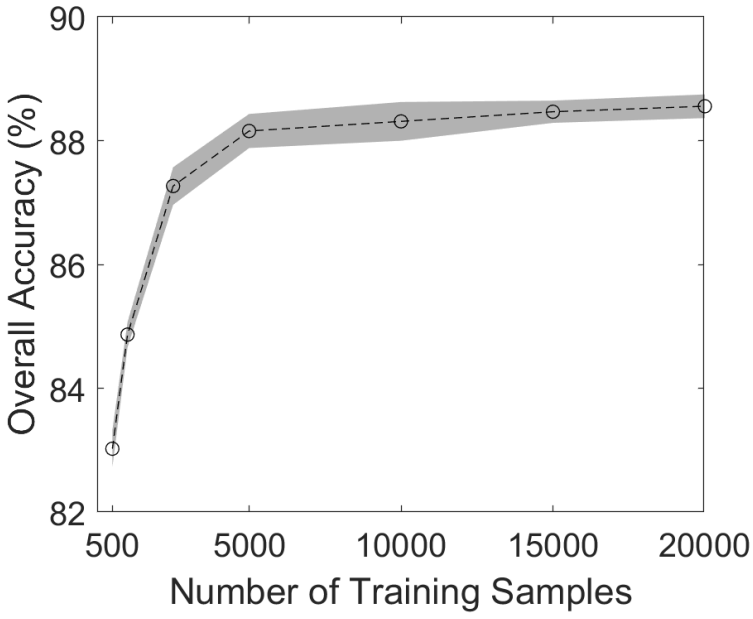

Figure 8. Impacts of the total number of training samples on the overall accuracy of land disturbance agent classification against the calibration samples.

3.4. Accuracy assessment

A confusion matrix, based on the stratified reference samples described in Section 2.5, will be created for the accuracy assessment of land disturbance agent maps. Then, we followed the approaches documented in (Olofsson et al., 2013) to compute a post-stratified estimator to translate the confusion matrix into terms of unbiased accuracies, such as producer's accuracy, user's accuracy, and overall accuracy. The uncertainty of the accuracy evaluation can be quantified by a confidence interval of 95%. We assumed that the bias in the area of mapped agents is uniformly distributed in time and space (Olofsson et al., 2016). This assumption implies that although our stratification was conducted based on the accumulated area of all 36 annual land disturbance maps (1985-2020), the unbiased estimator can be used for uncertainty estimation of the annual maps.

4. Results

The land disturbance agent maps over the five test sites (45 Landsat ARD tiles) were evaluated qualitatively and quantitatively.

4.1. Visual assessment of disturbance agent maps

In order to demonstrate the algorithm performance in characterizing land disturbances at a continuous spatial mode, we accumulated all annual land disturbance agent maps between 1985 and 2020 to show the land disturbances that occurred most recently, that is, a single pixel could be disturbed several times during the period of analysis, yet the map only displayed the latest disturbance event (Figure 9). For instance, Figure 9a showed the land disturbance agent map in

New England, where most of the area experienced *harvest*, especially in the Northeast area (e.g., Marine), and few *mechanical* disturbances particularly in or around the urban area (e.g., Metro Boston). According to the enlarged maps, ODACA successfully identified *harvest* (L1), *mechanical* (L2), *debris* caused by a tornado (L3), *stress* caused by the gypsy moth breakout in 2016 (L4). Figure 9b showed the land disturbance agent map at Southeast, where most of the disturbances were *harvest* (L1) (also see the green color area in Figure 9b), but this site was often attacked by hurricanes and tornados, both of which resulted in a large area of *debris* (L2 & L3). At the same time, *mechanical*, such as agricultural practice, usually occurred, with *hydrology* around the river (L4). Those different land disturbance agents were successfully distinguished by ODACA. Figure 9c represented the Great Plains, in which there was an extremely large area of cropland, and subsequently, the *mechanical* disturbances (e.g., agriculture practices) were found by ODACA (L1) (see red color in Figure 9c). In this site, ODACA can also identify the *fire* over grassland (L2), the *mechanical* in urban areas (e.g., urban modification) (L3), and the *hydrology* near the lake (L4). Figure 9d showed the land disturbance agent maps at Rocky Mountains, where the major land disturbances were *fire* (L1), *harvest* (L2), and *mechanical* (e.g., agricultural practice) (L3), with small amount of *stress* (e.g., beetle) (L4), and they were also successfully attributed by ODACA. Figure 9e showed the land disturbance agent map at Far West, where *mechanical* (L1) and *fire* (L2) often occurred with extremely high frequency. In this site, ODACA successfully identified *hydrology* in the Owens Lake (L3), which was a dry lake and often influenced by the upstream river, and the *other* over the grassland, which was caused by the year-to-year climate variability.

(a) New England

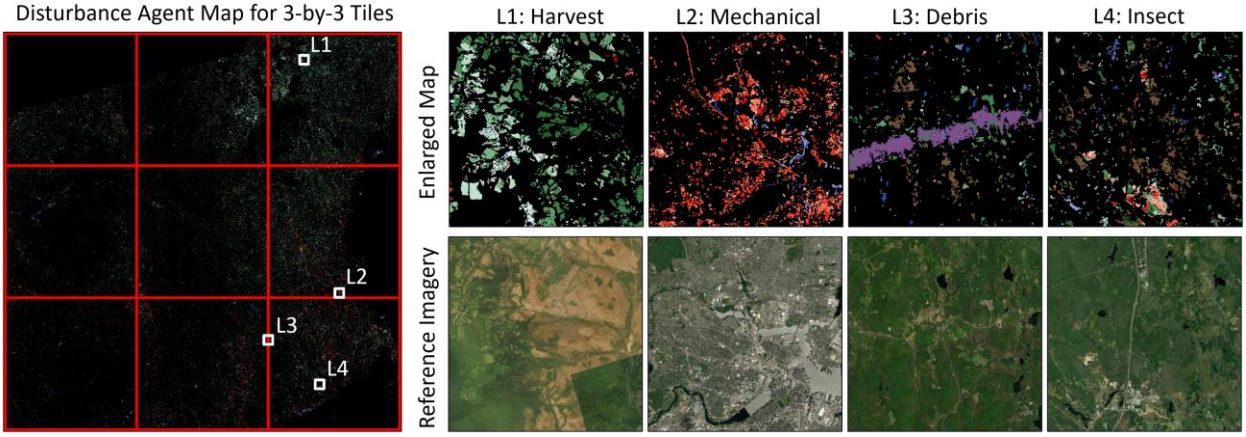

(b) Southeast

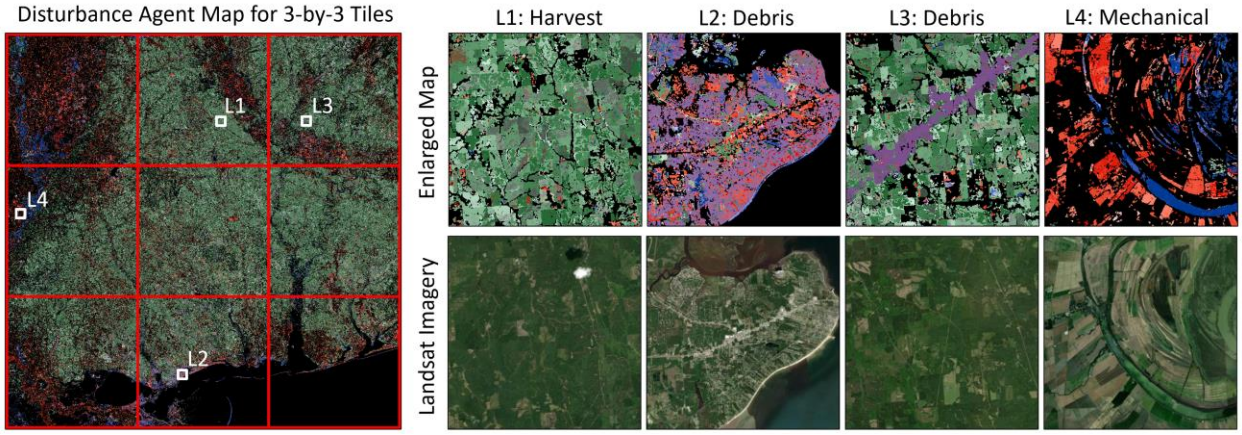

(c) Great Plains

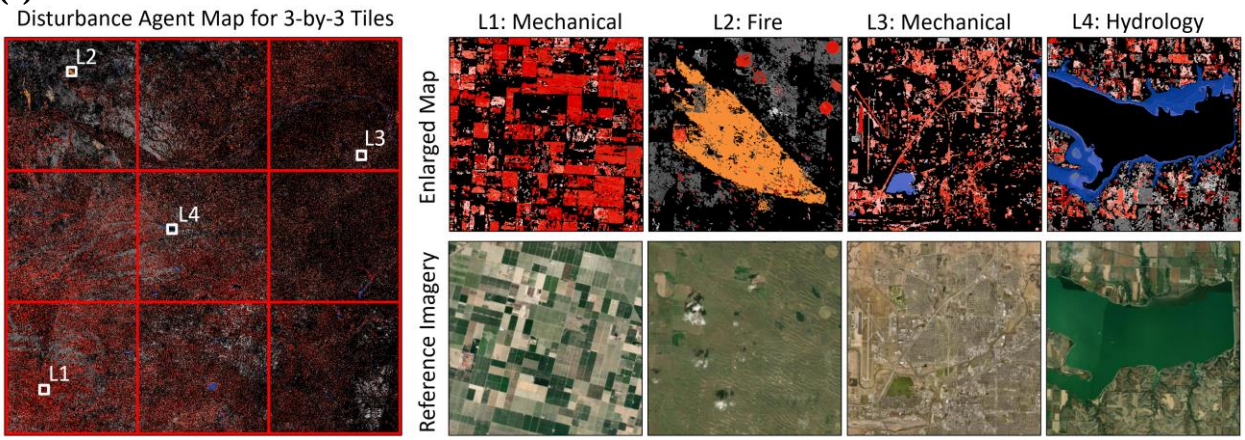

(d) Rocky Mountains

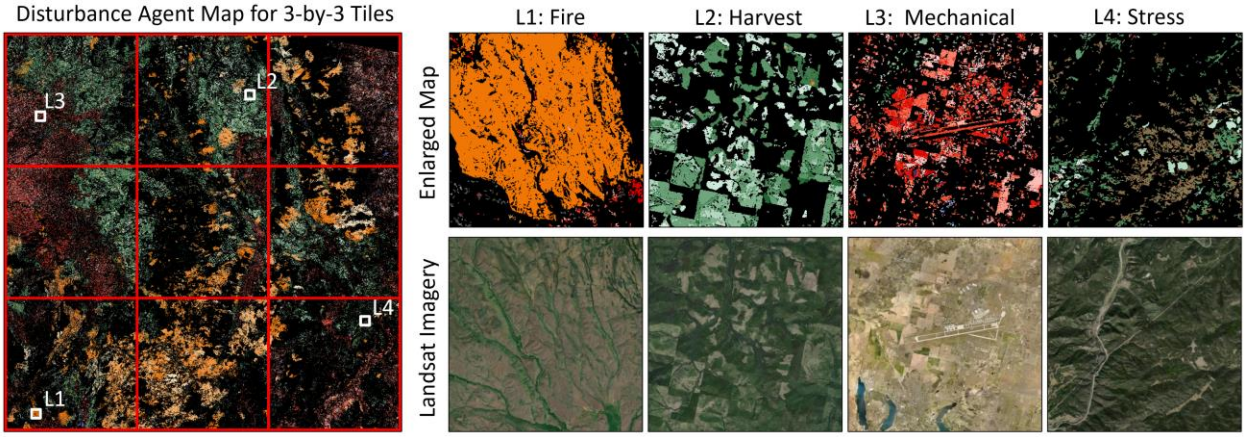

(e) Far West

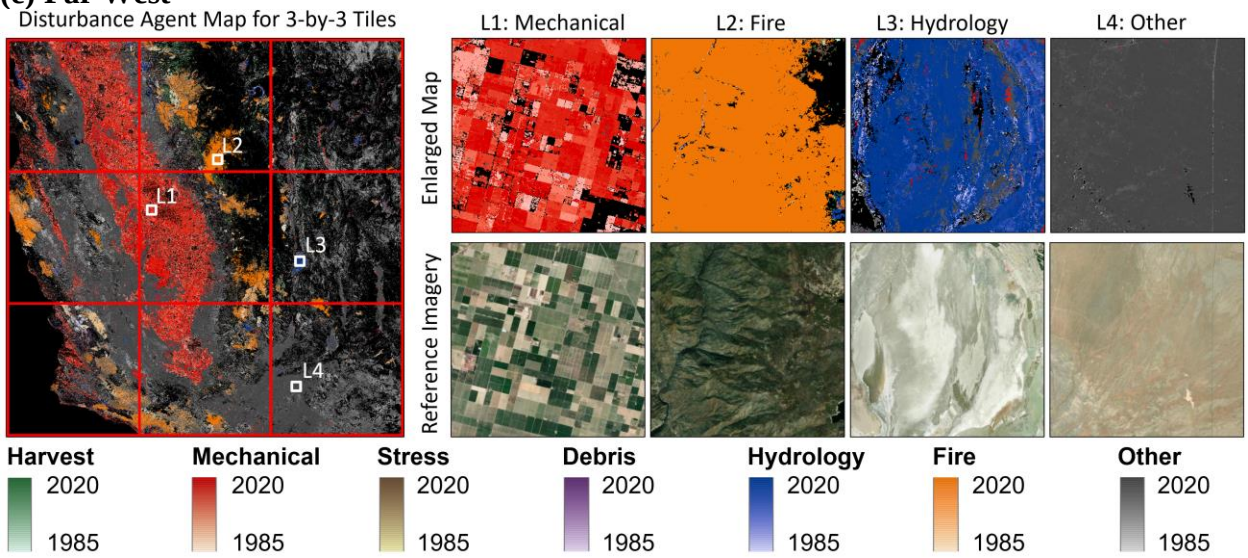

Figure 9. Accumulated land disturbance agent maps between 1985 and 2020 at (a) New England area (a), Southeast (b), Great Plains (c), Rocky Mountains (d), and Far West (e). At each site, there are 3-by-3 Landsat ARD tiles covered (red rectangles in the left large map), and enlarged examples are given at four different locations (L1, L2, L3, and L4). Color denotes the land disturbance agent, and brightness denotes the land disturbance time. The high-resolution reference images were derived from ArcMap software.

4.2. Quantitative assessment

Table 4 showed the accuracy assessment of the disturbance agent maps. The overall accuracy of the land disturbance agent classification was 99.68%. *No disturbance* achieved high user's and producer's accuracies (99.81% and 99.98%), which mostly benefited from the success of the COLD algorithm. Besides, most of the land disturbance agents, including *harvest*, *hydrology*, and *other*, also achieved high accuracies in both user's and producer's accuracy (> 90%), but *harvest* still had some commission errors from *debris* and *stress* because they share similar characteristics in spectral responses (e.g., decrease in NIR surface reflectance). At the same time, there were also confusions among *hydrology*, *other*, *mechanical,* and *debris*. The user's accuracy and producer's accuracy of *mechanical* were 93.94% and 76.20% (dominated by the commission errors with *no disturbance*), respectively. The user's accuracy of *fire* was higher than 95.70%, but its producer's accuracy was 80.46% because of commission errors contributed from *stress*, *debris*, and *harvest*. The user's accuracy and the producer's accuracy of *stress* were 68.42% and 60.82%, respectively, which are mainly caused by confusion in *harvest* (e.g., thinning) and low severity *fire*. The producer's accuracy of *debris* is very high (almost 100%), but its user's accuracy is relatively low (57.29%), mostly due to the large commission errors from *harvest* and *mechanical*.

Table 4

Confusion matrices and accuracy estimates for land disturbance agent map (with *no disturbance*). The reference samples and area estimations are displayed in columns and the map strata are displayed in rows. ± indicate the 95% confidence interval.

	No Disturbance	**Harvest**	**Mechanical**	**Stress**	**Debris**	**Hydrology**	**Fire**	**Other**
Confusion Matrix of Area Proportions (Unit: %)								
No Disturbance	97.22	0	0.19	0	0	0	0	0
Harvest	0	0.39	0	0	0	0	0.01	0
Mechanical	0.02	0	0.73	0	0	0	0	0.03
Stress	0	0	0	0.01	0	0	0	0
Debris	0	0.01	0	0	0.01	0	0	0
Hydrology	0	0	0	0	0	0.06	0	0
Fire	0	0	0	0	0	0	0.1	0
Other	0	0	0.04	0	0	0	0.01	1.15
Confusion Matrix of Sample Counts (Unit: Pixel)								
No Disturbance	524	0	1	0	0	0	0	0
Harvest	0	94	1	1	0	1	2	1
Mechanical	2	0	93	0	0	0	0	4
Stress	3	4	1	39	0	1	8	1
Debris	3	24	6	1	55	0	4	3
Hydrology	0	0	1	0	0	95	1	2
Fire	2	0	1	0	0	0	89	1
Other	0	0	3	0	0	0	1	96
Accuracy Estimates (Unit: %)								
Area Proportion	97.43±0.01	0.40±0.01	0.78±0.03	0.01±0.00	0.01±0.00	0.06±0.00	0.12±0.01	1.19±0.03
User's Accuracy	99.81±0.19	94.00±2.39	93.94±2.41	68.42±6.21	57.29±5.08	95.96±1.99	95.70±2.12	96.00±1.97
Producer's Accuracy	99.98±0.01	98.58±0.24	76.20±14.80	60.82±22.88	100.00±0.00	92.94±6.31	80.46±9.07	96.74±1.31
Overall Accuracy	99.68±0.19							

5. Discussions and conclusion

The new-developed ODACA can classify different kinds of land disturbance agents for five different sites across the United States by using the training data extracted from available open-source datasets. It is worth noting that though most of the training data are selected fully automated from the open-source datasets, they are also subject to errors and could be further improved if more human interpretations are provided to help with refining the training data. For example, we spent quite some time on refining the debris training data, but its large commission

error is still a major issue in our final disturbance agent map. In addition, all the predictor variables were used to produce land disturbance agent maps in this study; however, selection of the important predictor variables may benefit the computation efficiency for RFC-based classification tasks and improve classification accuracy when redundant variables are excluded (Chen et al., 2021; Sebald et al., 2021). Additionally, ODACA still faced misclassifications among *harvest*, *debris*, and *other* due to their similar spectral responses. The integration of auxiliary data such as weather reports, geological data, and social-environmental data (e.g., Twitter), are some of the future directions.

ODACA relies on the land disturbance detection results from the COLD algorithm, but COLD also has commission and omission errors in land disturbance detection (Zhu et al., 2020), and those errors will be inherited in the land disturbance agent maps. Methods that could combine the spatio-temporal information in change detection could potentially reduce the omission and commission of the COLD algorithm and provide more accurate land disturbance detection for ODACA to start with worth more future studies. In this study, we put climate variability into the *other* class, mostly because they are relatively ephemeral and have less long-term impact on the vegetation on the ground. This category, however, is not always interpreted as land change (Brown et al., 2020; Pengra et al., 2020) and is sometimes treated as commission errors in land disturbance detection. By putting them into the *other* category, we are able to reduce the commission error of the COLD algorithm, which is also the case for spectral changes caused by vegetation regrowth. On the other hand, omission errors of COLD are usually large for the small magnitude and ephemeral changes, such as *stress* caused by insect (Ye et al., 2021), and thus the use of the agent map of *stress* needs attention.

In conclusion, we implemented the modified COLD algorithm to detect land disturbance at a large-scale using Landsat time series from a single path and developed an Object-based Disturbance Agent Classification Approach (ODACA) for automated characterizing different kinds of land disturbance agents, with an overall accuracy of approximately 99% in the land disturbance agent map. The algorithms could potentially create CONUS-wide land disturbance agent products at 30-m resolution annually.

Acknowledgments

This work was supported by the USGS-NASA Landsat Science Team (LST) Program (#G17PS00256), and USGS Great Plains Cooperative Ecosystem Studies Unit (CESU) Program (#G17AC00057). The content of this document does not necessarily represent the views or policies of the Department of the Interior, nor does mention of trade names, commercial products or organizations imply endorsement by the U.S. Government.

Reference

Arévalo, P., Bullock, E.L., Woodcock, C.E., Olofsson, P., 2020. A Suite of Tools for Continuous Land Change Monitoring in Google Earth Engine. Frontiers in Climate 2, 1–19. https://doi.org/10.3389/fclim.2020.576740

Breiman, L., 2001. Random Forests. Machine Learning 45, 5–32.

Brown, J.F., Tollerud, H.J., Barber, C.P., Zhou, Q., Dwyer, J.L., Vogelmann, J.E., Loveland, T.R., Woodcock, C.E., Stehman, S.V., Zhu, Z., Pengra, B.W., 2020. Lessons learned implementing an operational continuous United States national land change monitoring

capability: The Land Change Monitoring, Assessment, and Project (LCMAP) approach. Remote Sensing of Environment 238, 111356. https://doi.org/10.1016/j.rse.2019.111356

Bullock, E.L., Woodcock, C.E., Holden, C.E., 2019. Improved change monitoring using an ensemble of time series algorithms. Remote Sensing of Environment 111165. https://doi.org/10.1016/j.rse.2019.04.018

Bullock, E.L., Woodcock, C.E., Souza, C., Olofsson, P., 2020. Satellite-based estimates reveal widespread forest degradation in the Amazon. Global Change Biology 26, 2956–2969. https://doi.org/10.1111/gcb.15029

Chen, B., Tu, Y., Song, Y., Theobald, D.M., Zhang, T., Ren, Z., Li, X., Yang, J., Wang, J., Wang, X., Gong, P., Bai, Y., Xu, B., 2021. Mapping essential urban land use categories with open big data: Results for five metropolitan areas in the United States of America. ISPRS Journal of Photogrammetry and Remote Sensing 178, 203–218. https://doi.org/https://doi.org/10.1016/j.isprsjprs.2021.06.010

Cohen, W.B., Healey, S.P., Yang, Z., Zhu, Z., Gorelick, N., 2020. Diversity of Algorithm and Spectral Band Inputs Improves Landsat Monitoring of Forest Disturbance. Remote Sensing 12. https://doi.org/10.3390/rs12101673

Coops, N.C., Shang, C., Wulder, M.A., White, J.C., Hermosilla, T., 2020. Change in forest condition: Characterizing non-stand replacing disturbances using time series satellite imagery. Forest Ecology and Management 474, 118370. https://doi.org/10.1016/j.foreco.2020.118370

Dobson, J.E., 1995. NOAA Coastal Change Analysis Program (C-CAP): guidance for regional implementation.

563 Dwyer, J., Roy, D., Sauer, B., Jenkerson, C., Zhang, H., Lymburner, L., 2018. Analysis Ready
564 Data: Enabling Analysis of the Landsat Archive 1–24.
565 https://doi.org/10.20944/PREPRINTS201808.0029.V1
566 Edwards, D.P., Tobias, J.A., Sheil, D., Meijaard, E., Laurance, W.F., 2014. Maintaining
567 ecosystem function and services in logged tropical forests. Trends in Ecology and Evolution
568 29, 511–520. https://doi.org/10.1016/j.tree.2014.07.003
569 Eidenshink, J., Schwind, B., Brewer, K., Zhu, Z., Quayle, B., Howard, S., Falls, S., Falls, S.,
570 2007. A Project for Monitoring Trends in Burn Severity. Fire Ecology 3, 3–21.
571 https://doi.org/10.4996/fireecology.0301003
572 Fan, C., Myint, S., 2014. A comparison of spatial autocorrelation indices and landscape metrics
573 in measuring urban landscape fragmentation. Landscape and Urban Planning 121, 117–128.
574 https://doi.org/https://doi.org/10.1016/j.landurbplan.2013.10.002
575 Gorelick, N., Hancher, M., Dixon, M., Ilyushchenko, S., Thau, D., Moore, R., 2017. Google
576 Earth Engine: Planetary-scale geospatial analysis for everyone. Remote Sensing of
577 Environment 202, 18–27. https://doi.org/https://doi.org/10.1016/j.rse.2017.06.031
578 Hansen, M.C., Egorov, A., Potapov, P. v, Stehman, S. v, Tyukavina, A., Turubanova, S.A., Roy,
579 D.P., Goetz, S.J., Loveland, T.R., Ju, J., 2014. Monitoring conterminous United States
580 (CONUS) land cover change with web-enabled Landsat data (WELD). Remote sensing of
581 Environment 140, 466–484.
582 Hansen, M.C., Potapov, P.V., Moore, R., Hancher, M., Turubanova, S.A.A., Tyukavina, A.,
583 Thau, D., Stehman, S.V., Goetz, S.J., Loveland, T.R., Kommareddy, A., 2013. High-
584 resolution global maps of 21st-century forest cover change. Science 342, 850–853.
585 https://doi.org/10.1126/science.1244693

Healey, S.P., Cohen, W.B., Yang, Z., Kenneth Brewer, C., Brooks, E.B., Gorelick, N., Hernandez, A.J., Huang, C., Joseph Hughes, M., Kennedy, R.E., Loveland, T.R., Moisen, G.G., Schroeder, T.A., Stehman, S. v., Vogelmann, J.E., Woodcock, C.E., Yang, L., Zhu, Z., 2018. Mapping forest change using stacked generalization: An ensemble approach. Remote Sensing of Environment 204, 717–728. https://doi.org/10.1016/j.rse.2017.09.029

Healey, S.P., Cohen, W.B., Zhiqiang, Y., Krankina, O.N., 2005. Comparison of Tasseled Cap-based Landsat data structures for use in forest disturbance detection. Remote Sensing of Environment 97, 301–310. https://doi.org/10.1016/j.rse.2005.05.009

Hermosilla, T., Wulder, M.A., White, J.C., Coops, N.C., Hobart, G.W., 2015a. An integrated Landsat time series protocol for change detection and generation of annual gap-free surface reflectance composites. Remote Sensing of Environment 158, 220–234. https://doi.org/10.1016/j.rse.2014.11.005

Hermosilla, T., Wulder, M.A., White, J.C., Coops, N.C., Hobart, G.W., 2015b. Regional detection, characterization, and attribution of annual forest change from 1984 to 2012 using Landsat-derived time-series metrics. Remote Sensing of Environment 170, 121–132. https://doi.org/10.1016/j.rse.2015.09.004

Hesselbarth, M.H.K., Sciaini, M., With, K.A., Wiegand, K., Nowosad, J., 2019. landscapemetrics: an open-source R tool to calculate landscape metrics. Ecography 42, 1648–1657. https://doi.org/10.1111/ecog.04617

Huang, C., Goward, S.N., Masek, J.G., Thomas, N., Zhu, Z., Vogelmann, J.E., 2010. An automated approach for reconstructing recent forest disturbance history using dense Landsat time series stacks. Remote Sensing of Environment 114, 183–198. https://doi.org/10.1016/j.rse.2009.08.017

609 Jin, S., Homer, C., Yang, L., Danielson, P., Dewitz, J., Li, C., Zhu, Z., Xian, G., Howard, D.,
610 2019. Overall methodology design for the United States national land cover database 2016
611 products. Remote Sensing 11. https://doi.org/10.3390/rs11242971
612 Johnson, E.W., Wittwer, D., 2008. Aerial detection surveys in the United States. Australian
613 Forestry 71, 212–215. https://doi.org/10.1080/00049158.2008.10675037
614 Kennedy, R.E., Cohen, W.B., Schroeder, T.A., 2007. Trajectory-based change detection for
615 automated characterization of forest disturbance dynamics. Remote Sensing of Environment
616 110, 370–386. https://doi.org/https://doi.org/10.1016/j.rse.2007.03.010
617 Kennedy, R.E., Yang, Z., Braaten, J., Copass, C., Antonova, N., Jordan, C., Nelson, P., 2015.
618 Attribution of disturbance change agent from Landsat time-series in support of habitat
619 monitoring in the Puget Sound region, USA. Remote Sensing of Environment 166, 271–
620 285. https://doi.org/10.1016/j.rse.2015.05.005
621 Kennedy, R.E., Yang, Z., Cohen, W.B., 2010. Detecting trends in forest disturbance and
622 recovery using yearly Landsat time series: 1. LandTrendr—Temporal segmentation
623 algorithms. Remote Sensing of Environment 114, 2897–2910.
624 https://doi.org/https://doi.org/10.1016/j.rse.2010.07.008
625 Kirschbaum, D.B., Adler, R., Hong, Y., Hill, S., Lerner-Lam, A., 2010. A global landslide
626 catalog for hazard applications: method, results, and limitations. Natural Hazards 52, 561–
627 575. https://doi.org/10.1007/s11069-009-9401-4
628 Loveland, T.R., Sohl, T.L., Stehman, S. V, Gallant, A.L., Sayler, K.L., Napton, D.E., 2002. A
629 strategy for estimating the rates of recent United States land-cover changes.
630 Photogrammetric Engineering and Remote Sensing 68, 1091–1099.

631 Masek, J.G., Vermote, E.F., Saleous, N.E., Wolfe, R., Hall, F.G., Huemmrich, K.F., Gao, F.,
632 Kutler, J., Lim, T.-K., 2006. A Landsat surface reflectance dataset for North America, 1990-
633 2000. IEEE Geoscience and Remote Sensing Letters 3, 68–72.
634 https://doi.org/10.1109/LGRS.2005.857030
635 Oeser, J., Pflugmacher, D., Senf, C., Heurich, M., Hostert, P., 2017. Using intra-annual Landsat
636 time series for attributing forest disturbance agents in Central Europe. Forests 8, 251.
637 https://doi.org/https://doi.org/10.3390/f8070251
638 Olofsson, P., Foody, G.M., Herold, M., Stehman, S. V., Woodcock, C.E., Wulder, M.A., 2014.
639 Good practices for estimating area and assessing accuracy of land change. Remote Sensing
640 of Environment 148, 42–57. https://doi.org/10.1016/j.rse.2014.02.015
641 Olofsson, P., Foody, G.M., Stehman, S. V., Woodcock, C.E., 2013. Making better use of
642 accuracy data in land change studies: Estimating accuracy and area and quantifying
643 uncertainty using stratified estimation. Remote Sensing of Environment 129, 122–131.
644 https://doi.org/10.1016/j.rse.2012.10.031
645 Olofsson, P., Holden, C.E., Bullock, E.L., Woodcock, C.E., 2016. Time series analysis of
646 satellite data reveals continuous deforestation of New England since the 1980s.
647 Environmental Research Letters 11. https://doi.org/10.1088/1748-9326/11/6/064002
648 Pekel, J.-F., Cottam, A., Gorelick, N., Belward, A.S., 2016. High-resolution mapping of global
649 surface water and its long-term changes. Nature 540, 418–422.
650 https://doi.org/10.1038/nature20584
651 Pengra, B.W., Stehman, S. v., Horton, J.A., Dockter, D.J., Schroeder, T.A., Yang, Z., Cohen,
652 W.B., Healey, S.P., Loveland, T.R., 2020. Quality control and assessment of interpreter
653 consistency of annual land cover reference data in an operational national monitoring

654 program. Remote Sensing of Environment 238, 111261.
655 https://doi.org/10.1016/j.rse.2019.111261
656 Rodriguez, E., Morris, C.S., Belz, J.E., 2006. A global assessment of the SRTM performance.
657 Photogrammetric Engineering & Remote Sensing 72, 249–260.
658 Rodriguez-Galiano, V.F., Ghimire, B., Rogan, J., Chica-Olmo, M., Rigol-Sanchez, J.P., 2012.
659 An assessment of the effectiveness of a random forest classifier for land-cover
660 classification. ISPRS journal of photogrammetry and remote sensing 67, 93–104.
661 Rollins, M.G., 2009. LANDFIRE: A nationally consistent vegetation, wildland fire, and fuel
662 assessment. International Journal of Wildland Fire 18, 235–249.
663 https://doi.org/10.1071/WF08088
664 Roy, D.P., Huang, H., Boschetti, L., Giglio, L., Yan, L., Zhang, H.H., Li, Z., 2019. Landsat-8
665 and Sentinel-2 burned area mapping - A combined sensor multi-temporal change detection
666 approach. Remote Sensing of Environment 231, 111254.
667 https://doi.org/10.1016/j.rse.2019.111254
668 Schroeder, T.A., Schleeweis, K.G., Moisen, G.G., Toney, C., Cohen, W.B., Freeman, E.A.,
669 Yang, Z., Huang, C., 2017. Testing a Landsat-based approach for mapping disturbance
670 causality in U.S. forests. Remote Sensing of Environment 195, 230–243.
671 https://doi.org/10.1016/j.rse.2017.03.033
672 Sebald, J., Senf, C., Seidl, R., 2021. Human or natural? Landscape context improves the
673 attribution of forest disturbances mapped from Landsat in Central Europe. Remote Sensing
674 of Environment 262, 112502. https://doi.org/https://doi.org/10.1016/j.rse.2021.112502
675 States, U., 1995. FRAGSTATS: Spatial Pattern Analysis Program for Quantifying Landscape
676 Structure.

677 Tibshirani, R., 2011. Regression shrinkage and selection via the lasso: a retrospective. Journal of
678 the Royal Statistical Society: Series B (Statistical Methodology) 73, 273–282.
679 Turner II, B.L., Lambin, E.F., Reenberg, A., 2007. The emergence of land change science for
680 global environmental change and sustainability.
681 van Mantgem, P.J., Stephenson, N.L., Byrne, J.C., Daniels, L.D., Franklin, J.F., Fulé, P.Z.,
682 Harmon, M.E., Larson, A.J., Smith, J.M., Taylor, A.H., Veblen, T.T., 2009. Widespread
683 increase of tree mortality rates in the Western United States. Science 323, 521–524.
684 https://doi.org/10.1126/science.1165000
685 Verbesselt, J., Zeileis, A., Herold, M., 2012. Near real-time disturbance detection using satellite
686 image time series. Remote Sensing of Environment 123, 98–108.
687 https://doi.org/https://doi.org/10.1016/j.rse.2012.02.022
688 Vermote, E., Justice, C., Claverie, M., Franch, B., 2016. Preliminary analysis of the performance
689 of the Landsat 8/OLI land surface reflectance product. Remote Sensing of Environment
690 185, 46–56. https://doi.org/10.1016/j.rse.2016.04.008
691 Woodcock, C.E., Allen, R., Anderson, M., Belward, A., Bindschadler, R., Cohen, W., Gao, F.,
692 Goward, S.N., Helder, D., Helmer, E., Nemani, R., Oreopoulos, L., Schott, J., Thenkabail,
693 P.S., Vermote, E.F., Vogelmann, J., Wulder, M.A., Wynne, R., 2008. Free access to
694 Landsat imagery. Science 320, 1011–1011. https://doi.org/10.1126/science.320.5879.1011a
695 Wulder, M.A., Masek, J.G., Cohen, W.B., Loveland, T.R., Woodcock, C.E., 2012. Opening the
696 archive: How free data has enabled the science and monitoring promise of Landsat. Remote
697 Sensing of Environment 122, 2–10. https://doi.org/10.1016/j.rse.2012.01.010

698 Xian, G.Z., Smith, K., Wellington, D., Horton, J., Zhou, Q., Li, C., Auch, R., Brown, J.F., Zhu,
699 Z., Reker, R.R., 2022. Implementation of the CCDC algorithm to produce the LCMAP
700 Collection 1.0 annual land surface change product. Earth System Science Data 14, 143–162.
701 Ye, S., Rogan, J., Zhu, Z., Hawbaker, T.J., Hart, S.J., Andrus, R.A., Meddens, A.J.H., Hicke,
702 J.A., Eastman, J.R., Kulakowski, D., 2021. Detecting subtle change from dense Landsat
703 time series: Case studies of mountain pine beetle and spruce beetle disturbance. Remote
704 Sensing of Environment 263, 112560.
705 https://doi.org/https://doi.org/10.1016/j.rse.2021.112560
706 Zhang, Y., Woodcock, C.E., Chen, S., Wang, J.A., Sulla-Menashe, D., Zuo, Z., Olofsson, P.,
707 Wang, Y., Friedl, M.A., 2022. Mapping causal agents of disturbance in boreal and arctic
708 ecosystems of North America using time series of Landsat data. Remote Sensing of
709 Environment 272, 112935. https://doi.org/10.1016/j.rse.2022.112935
710 Zhe, Z., Shi, Q., 2022. Remote Sensing of Land Change: A Multifaceted Perspective. Preprint.
711 https://doi.org/10.1002/essoar.10510470.1
712 Zhou, Q., Rover, J., Brown, J., Worstell, B., Howard, D., Wu, Z., Gallant, A.L., Rundquist, B.,
713 Burke, M., 2019. Monitoring landscape dynamics in central U.S. grasslands with
714 harmonized Landsat-8 and Sentinel-2 time series data. Remote Sensing 11, 328.
715 https://doi.org/10.3390/rs11030328
716 Zhu, Z., Gallant, A.L., Woodcock, C.E., Pengra, B., Olofsson, P., Loveland, T.R., Jin, S., Dahal,
717 D., Yang, L., Auch, R.F., 2016. Optimizing selection of training and auxiliary data for
718 operational land cover classification for the LCMAP initiative. ISPRS Journal of
719 Photogrammetry and Remote Sensing 122, 206–221.
720 https://doi.org/10.1016/j.isprsjprs.2016.11.004

721 Zhu, Z., Wang, S., Woodcock, C.E., 2015. Improvement and expansion of the Fmask algorithm:
722 Cloud, cloud shadow, and snow detection for Landsats 4-7, 8, and Sentinel 2 images.
723 Remote Sensing of Environment 159, 269–277. https://doi.org/10.1016/j.rse.2014.12.014
724 Zhu, Z., Woodcock, C.E., 2014. Continuous change detection and classification of land cover
725 using all available Landsat data. Remote Sensing of Environment 144, 152–171.
726 https://doi.org/10.1016/j.rse.2014.01.011
727 Zhu, Z., Woodcock, C.E., Olofsson, P., 2012. Continuous monitoring of forest disturbance using
728 all available Landsat imagery. Remote Sensing of Environment 122, 75–91.
729 https://doi.org/10.1016/j.rse.2011.10.030
730 Zhu, Z., Wulder, M.A., Roy, D.P., Woodcock, C.E., Hansen, M.C., Radeloff, V.C., Healey, S.P.,
731 Schaaf, C., Hostert, P., Strobl, P., Pekel, J.F., Lymburner, L., Pahlevan, N., Scambos, T.A.,
732 2019. Benefits of the free and open Landsat data policy. Remote Sensing of Environment
733 224, 382–385. https://doi.org/10.1016/j.rse.2019.02.016
734 Zhu, Z., Zhang, J., Yang, Z., Aljaddani, A.H., Cohen, W.B., Qiu, S., Zhou, C., 2020. Continuous
735 monitoring of land disturbance based on Landsat time series. Remote Sensing of
736 Environment 238, 111116. https://doi.org/10.1016/j.rse.2019.03.009
737
738